Effect of Oriented Assemblies of $SrTiO_3$ with Exposed (200) plane on the Photocatalytic Hydrogen Evolution

Aditi Vijay[a], Shanmuga Priya S[a], Dr. Umberto Terranova[b], Madhusudan Maity[c], Dr. Sonalika Vaidya[a]*

[a] Institute of Nano Science and Technology, Knowledge City, Sector 81, Sahibzada Ajit Singh Nagar, Punjab 140306, India

[b] Faculty of Medicine and Health Science, Crewe Campus, University of Buckingham, Crewe, CW1 5DU, United Kingdom

[c] Department of Chemical Sciences, Indian Institute of Science Education and Research (IISER) Mohali, Sector-81, Sahibzada Ajit Singh Nagar, Knowledge City, Manauli 140306, India

Corresponding Author: svaidya@inst.ac.in; https://inst.ac.in/scientist/38

Abstract

This study aims to investigate the effect of crystallographic orientation of the assemblies of $SrTiO_3$ (formed on a glass substrate) on photocatalytic hydrogen evolution. For this, we have successfully synthesized nanocubes of $SrTiO_3$ through the hydrothermal method. Assemblies on the glass substrate were formed by using functionalized/non-functionalized oxide over functionalized/nonfunctionalized glass substrate. The functionalization of the oxides and the glass substrate was carried out using IPTMS (3-iodopropyltrimethoxy silane). Uniform assemblies of nanocubes of $SrTiO_3$ with the particles oriented with (200) plane as the exposed surface were formed. The performance of these oriented assemblies was evaluated for photocatalytic hydrogen evolution reaction. Theoretical studies were carried out to understand the mechanism of photocatalytic hydrogen evolution over the oriented assemblies of $SrTiO_3$.

Introduction

The development of a clean and green source of energy is considered an effective method to tackle issues related to energy and environment. In this regard, Hydrogen is considered an alternative source of energy as it can be produced using renewable resources. In recent years, Photocatalytic water-splitting has emerged as an effective technique to produce hydrogen from water using solar energy[1]. So far, many efforts have been made to improve the efficiency of the catalyst by reducing the size[2], varying the morphology[3], modulating the surfaces and interfaces of a photocatalyst[4], controlling the exposed facets[5], etc. It is known that assemblies exhibit unique electrical, optical, magnetic, and catalytic properties not only because of the increase in surface-to-volume ratio but also because of the emergence of collective property as a result of interparticle arrangement or assembly. In addition to the approaches to alter the physical properties, it has been observed that crystallographic orientation also plays an important role in catalysis. For instance, 3D assembly of highly oriented nanocubes of $SrTiO_3$ with size 60−80 nm were formed by the partial sharing of (100) faces[6]. These assemblies were found to exhibit enhanced photocatalytic activity towards hydrogen evolution from water splitting. Crystallographically oriented thin films of rutile on sapphire and rutile substrate were synthesized by Hotsenpiller et.al.[7] for the photochemical reduction of Ag^+ to Ag metal on rutile surfaces. Films grown along the (001) plane were found to be the most active for photoreduction. Guoqiang Li et. al [8] studied catalytic activity of thin films of WO_3 having a preferred orientation along (001), (110), and (111) planes grown on $LaAlO_3$ substrate. It was observed that the rate of photodegradation of RhB dye was affected by the orientation of the planes and was found to follow the order (111) > (110) > (001). In another report[9] by Guoqiang Li ,wherein films of $NaNbO_3$ with preferred orientation along (100), (110), and (111) crystal planes were grown on (100), (110), and (111) $LaAlO_3$ substrate, the photocatalytic activity (for the degradation of Rhodamine B (RhB) dye) was found to be maximum for the $NaNbO_3$ films oriented along (111) crystal plane on $LaAlO_3$ substrate. Photocatalytic activity is shown to depend on the coercive electric field. Higher is the field lower is the activity. Linqin Jiang et.al[10] reported that assembly of $NaNbO_3$ along the b-axis, (an axis possessing an internal bias electric field along this direction) showed enhanced photocatalytic activity than the disordered $NaNbO_3$ nanostructures. It has been observed[11] for $NaNbO_3$ deposited on $SrTiO_3$ substrates that the coercive electric field decreases with the following orientations of the film: (100) > (110) > (111). Films of Nb-doped TiO_2 (powder synthesized using plasma technique) were formed in

presence of a magnetic field using the slip casting method by Chenning Zhang et al.[12]. They observed that the activity of the catalyst for photocatalytic degradation of methyl orange dye was found to show improved performance for (001) oriented Nb-doped TiO_2. In addition to the photocatalytic activity, photoelectrochemical activity is also influenced by the crystallographic orientation of nanostructures. For instance, [010]-orientated $BiVO_4$ films were found to be more efficient as photoanodes in photoelectrochemical water splitting in comparison to [121]-orientated $BiVO_4$ films.[13]

Keeping the above factors (crystallographic orientation and exposed facets) into consideration, we have synthesized oriented assemblies of nanocubes of $SrTiO_3$ nanoparticles on the glass substrate using IPTMS (3-iodopropyltrimethoxy silane) as a linker between the glass substrate and $SrTiO_3$. $SrTiO_3$ has a wide bandgap of around 3.2 eV. The photocatalytic activity of $SrTiO_3$ could be enhanced by doping with metal cations or by defect engineering. Different morphologies of $SrTiO_3$ such as nanocubes[14], dodecahedron[15], flower[16], and star-like shape[17] have been reported for improving photocatalytic water splitting. The dependence of exposed crystal facets of $SrTiO_3$ on photocatalytic activity was also established. Bin Wang et. al.[5] showed that the {001} facet of $SrTiO_3$ was found to be active for photoreduction whereas the {023} facet was active for photooxidation reaction. Wu et. al[18] observed that photocatalytic oxidation activity on {110} exposed facet of $SrTiO_3$ was higher when compared with {001} facet exposed $SrTiO_3$. In a previous report of ours[19], we observed higher photocatalytic hydrogen evolution activity for $SrTiO_3$ having [100] exposed facet. In this study, the effect of assemblies on photocatalytic hydrogen evolution was studied. Theoretical studies were carried out to understand the mechanism of photocatalytic hydrogen evolution over the oriented assemblies of $SrTiO_3$. To the best of our knowledge, there is no report of photocatalytic hydrogen evolution using oriented assemblies of $SrTiO_3$ on the glass substrate as photocatalyst. We believe our work on relating photocatalytic activity with crystallographically oriented assemblies on glass substrate would further add to the field of designing nanostructures for photocatalytic hydrogen evolution.

Results and Discussion

As synthesized $SrTiO_3$ nanostructures

PXRD studies of $SrTiO_3$ nanostructures (Figure 1a) showed the formation of a pure phase wherein all the reflection planes could be indexed to the cubic unit cell (JCPDS card no.00-035-0734) having space group, $Pm\bar{3}m$. TEM study of $SrTiO_3$ nanostructures shows the formation of nanocubes having an average size of ~70 nm (Figure 1b). The size distribution obtained from TEM study is shown in Figure 1c and was found to range from ~50-90 nm. These nanocubes were further used for the formation of assemblies on a glass substrate under different conditions.

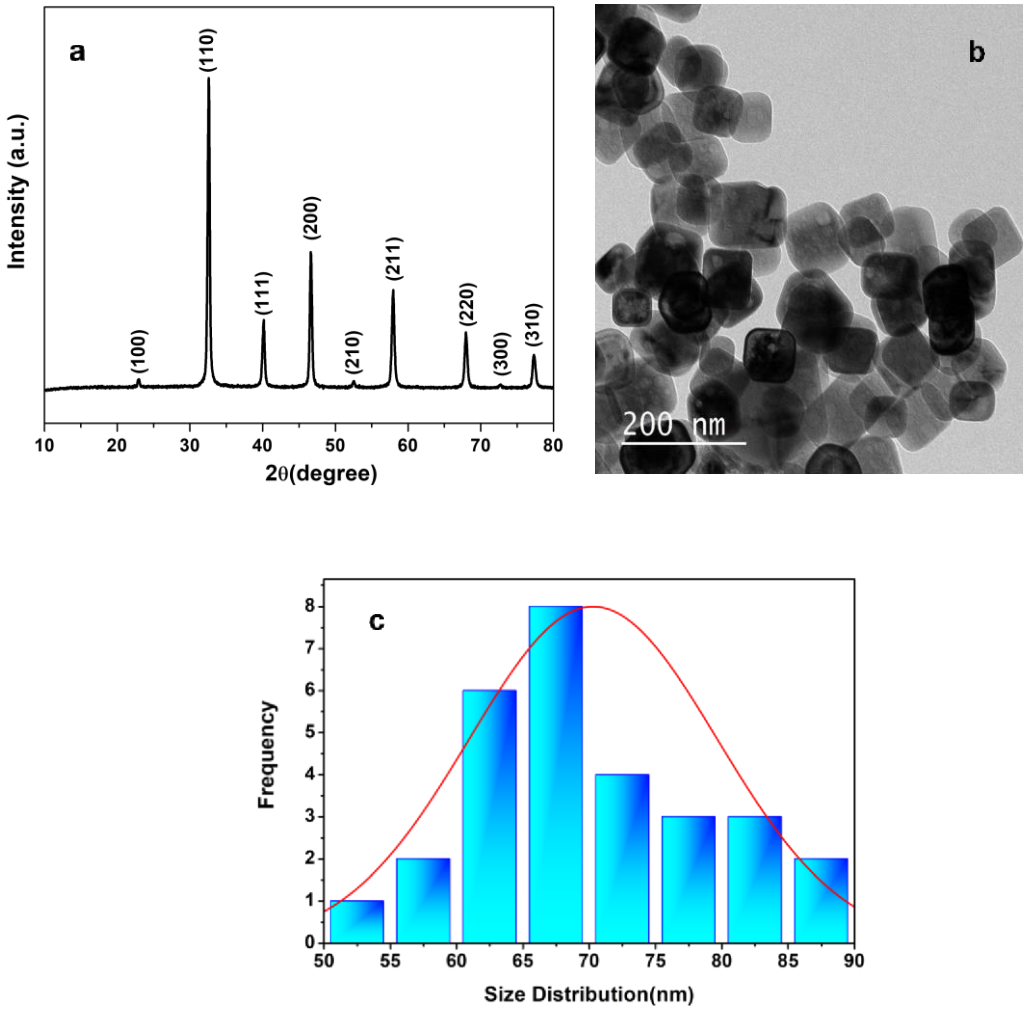

Figure 1: (a) PXRD pattern, (b) TEM image, and (c) Size distribution of $SrTiO_3$.

The high-resolution XPS spectra of $SrTiO_3$ are shown in Figure 2. Peaks at the binding energy corresponding to Sr $3d_{5/2}$ and Sr $3d_{3/2}$ were observed at 132.4 eV and 134.1 eV respectively in the Sr (3d) spectra (Figure 2a). Presence of Ti^{3+} (456.8 ($2p_{3/2}$) and 462.3 eV ($2p_{1/2}$)) along with Ti^{4+}

(457.8 ($2p_{3/2}$) and 463.7 eV ($2p_{1/2}$)) were observed after fitting of the high resolution spectra of Ti (2p) (Figure 2b). Two Gaussian peaks with a binding energy at 528.9 and 530.5 eV (Figure 2c) corresponding to metal –oxygen bond i.e. the presence of O^{2-} ions in the crystal structure and the presence of defect arising due to oxygen vacancy in $SrTiO_3$ respectively were observed in the high–resolution O1s spectra for the oxide. The presence of vacancy can also be correlated to the fact that Ti^{3+} is observed along with Ti^{4+} which can arise only due to oxygen vacancies in the sample. Thus the presence of a peak corresponding to oxygen vacancy along with Ti^{3+} confirms the presence of oxygen vacancy in the lattice. Such confirmation about the presence of oxygen vacancies and Ti^{3+} are also reported in the literature. For example, Bharti et.al [20] reported the presence of Ti^{3+} in the TiO_2 thin film after plasma treatment. The presence of oxygen vacancy or removal of lattice oxygen was confirmed from the increase in the peak area of the peak positioned at 531.5 eV in the O1s spectra. Zhang et.al[21] also observed peak corresponding to Ti^{3+} in the XPS spectra of Ti (2p) and a peak at 531.5 eV in the O 1s spectra corresponding to oxygen vacancy, in TiO_2 nanotubes. Presence of oxygen vacancies was also confirmed by Tan et.al[22] based on peak at 531.9 eV in the O1s spectra of $SrTiO_3$. We have also observed the presence of Ti^{3+} in the Ti 2p spectra and a peak at 530.5 eV in the O 1s spectra, confirming the presence of oxygen vacancies in $SrTiO_3$ nanostructures that were used for the formation of assemblies on the glass substrate.

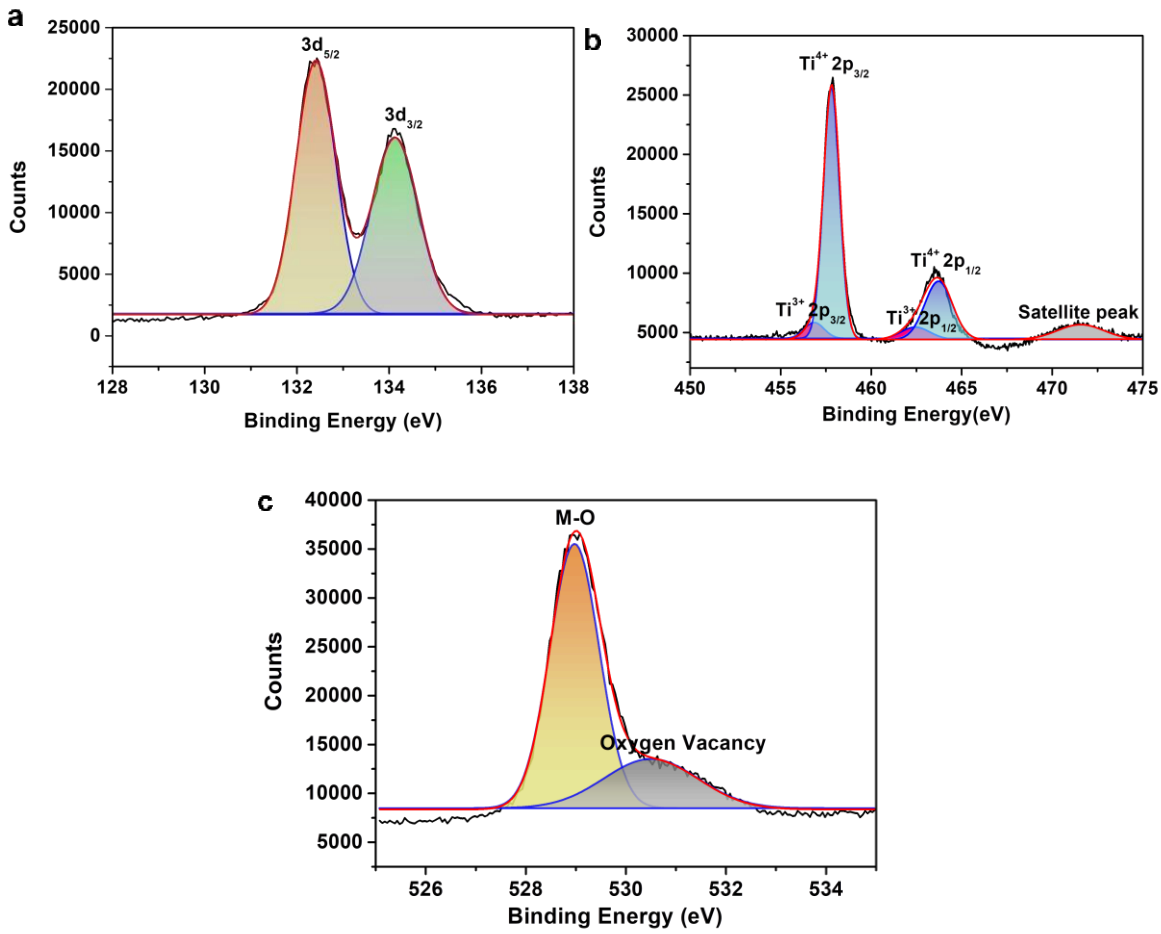

Figure 2: High Resolution (a) Sr (3d), (b) Ti (2p) and (c) O (1s) XPS spectra of $SrTiO_3$ nanostructures.

Assemblies of $SrTiO_3$ nanocubes on a glass substrate

To see the effect of assemblies on the orientation of the nanostructures on the glass substrate, XRD studies were carried out on STO-F1-STO-F4 (Figure 3). Three peaks corresponding to (100), (110), and (200) planes were observed in the XRD pattern of STO-F1 and STO-F2. It was observed that the intensity of the (200) plane was higher than that of the (110) plane which was different from the conventional pattern of intensity for $SrTiO_3$ wherein the intensity of the (110) plane is higher than the (200) plane. This suggests that the particles were oriented preferably with (200) as the exposed surface in STO-F1 and STO-F2. It is thus quite interesting to observe that the intensity of the (200) plane is enhanced for assemblies wherein the glass substrate was functionalized with IPTMS. However, in STO-F2, the intensity of the (200) plane was found to be much higher than

the (110) plane in comparison to the intensity difference between the two planes observed for STOF1. Such increase in the intensity of the (200) plane was also observed by Ma et.al[23] for oriented assemblies of $SrTiO_3$ formed on a glass substrate. In the case of STO-F3 and STO-F4, two peaks corresponding to (110) and (200) planes were observed. The intensity of the (200) plane was found to be lower than that of the (110) plane as is usually observed for $SrTiO_3$. This also suggests that there was no preference for (200) plane in STO-F3 and STO-F4.

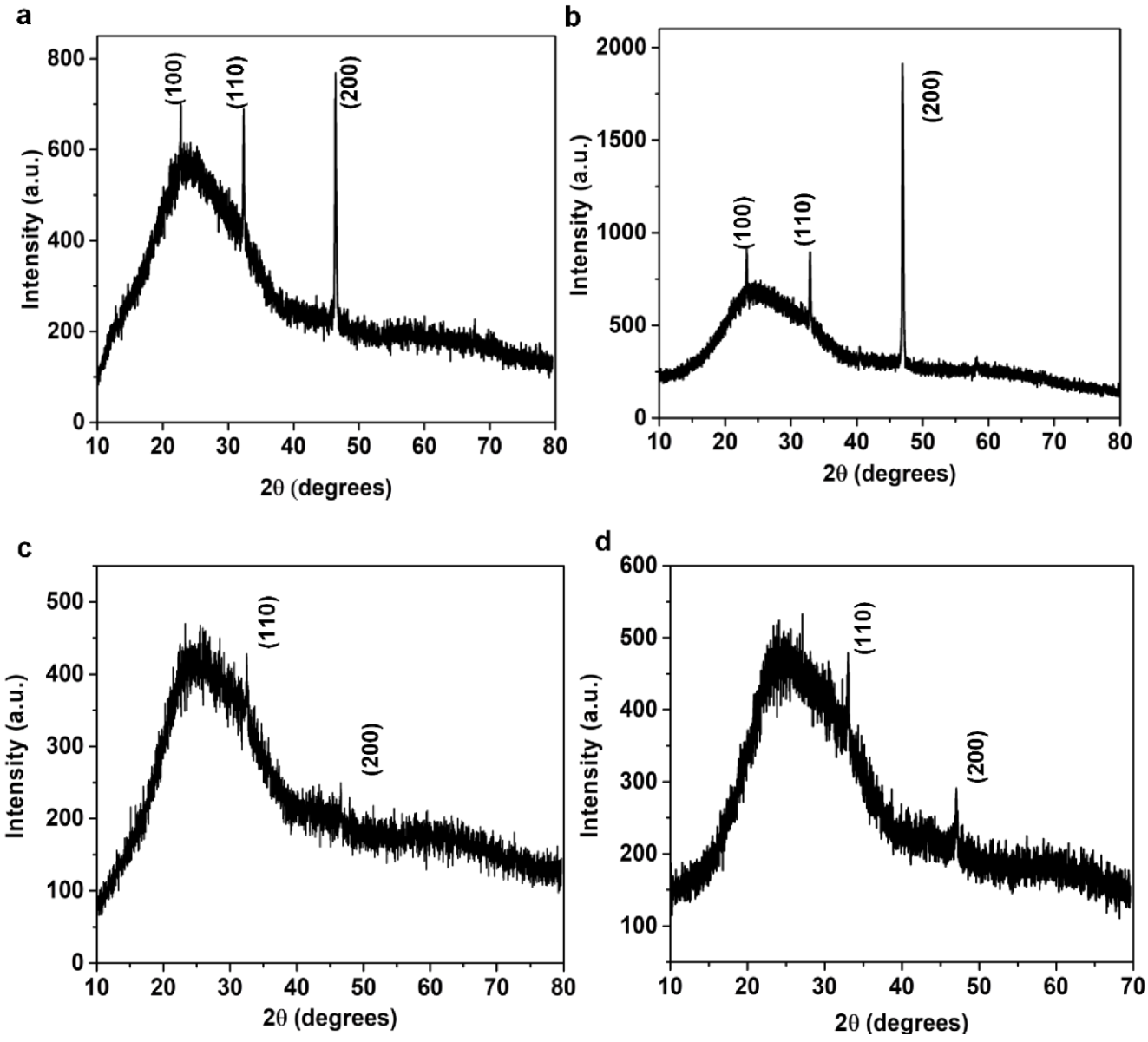

Figure 3: XRD pattern of (a) STO-F1, (b) STO-F2, (c) STO-F3, and (d) STO-F4.

To see the nature of assemblies of $SrTiO_3$ nanocubes on glass substrate for STO-F1-STO-F4, FESEM studies were carried out (Figure 4). At lower magnification, we observed a uniform distribution of the $SrTiO_3$ nanocubes with a maximum degree of coverage on the glass substrate

for STO-F2 which was fabricated by deposition of the non-functionalized nanocubes over IPTMSfunctionalized glass substrate (Figure 4b). The thickness of the deposited film in STO-F2 was measured through cross-sectional FESEM and was observed to be ~300 nm (Figure S1, ESI). This uniform kind of assembly were not observed for STO-F1 (Figure 4a), STO-F3 (Figure 4c), and STO-F4 (Figure 4d), though the coverage of nanocubes was more for STO-F3 and STO-F4 amongst the three kinds of assemblies (STO-F1, STO-F3, and STO-F4). However, the particles were observed to be agglomerated forming clusters in STO-F1, STO-F3, and STO-F4. A schematic showcasing a plausible mechanism for the formation of assemblies of $SrTiO_3$ on glass substrate for STO-F1 to STO-F4 is shown in Figure 5. It was observed that the non-functionalization of the oxide with IPTMS helped in maximum coverage of the nanocubes over the substrate (as observed for STO-F2 and STO-F4), though functionalizing the glass substrate helped in the formation of a uniform assembly. Agglomeration of particles in STO-F1 and STO-F3 could be explained by the fact that the oxide nanostructures were functionalized with IPTMS, which could have resulted in an interaction of the deposited nanostructures with other functionalized nanostructures, resulting in an agglomerated cluster. The agglomeration in STO-F4, wherein the particles were not functionalized, could be due to the effect of evaporation of the solvent after deposition.

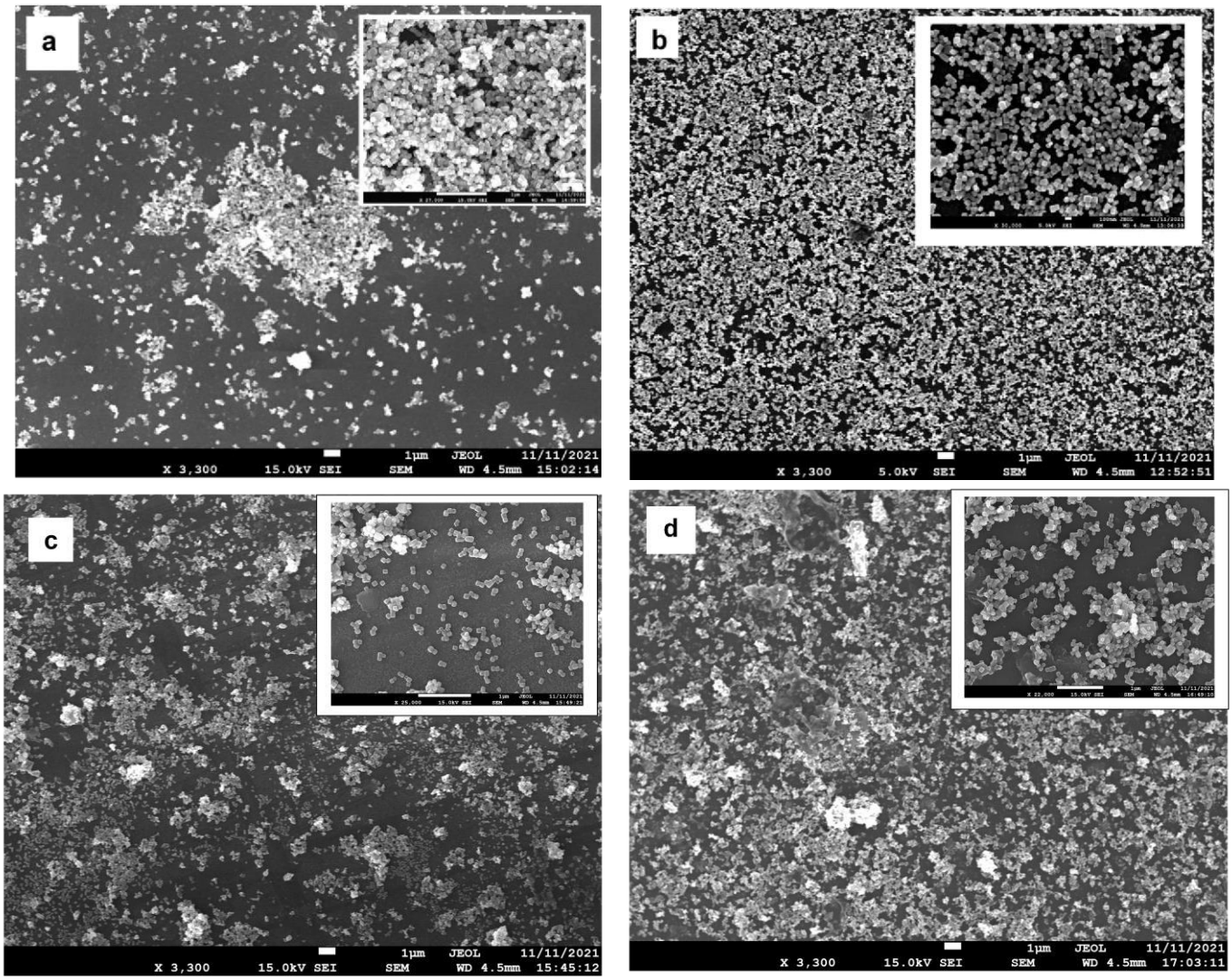

Figure 4: FESEM images of (a) STO-F1, (b) STO-F2, (c) STO-F3, and (d) STO-F4. Inset shows high magnification images.

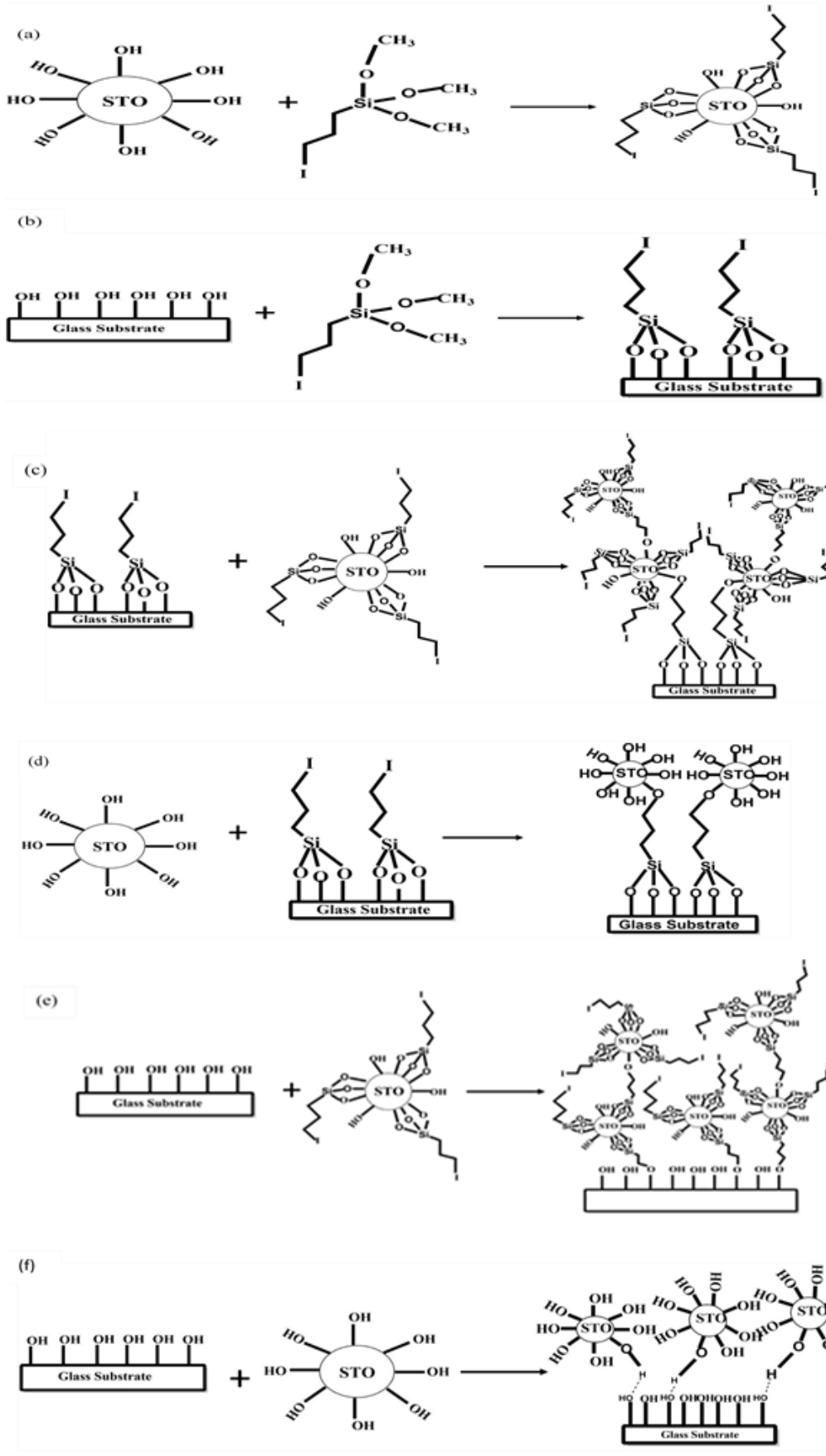
(a)
STO
(b)
Glass Substrate
(c)
Glass Substrate
(d)
Glass Substrate
(e)
Glass Substrate
(f)
Glass Substrate

Figure 5: Schematic showcasing (a) functionalization of $SrTiO_3$ nanostructures, (b) functionalization of glass substrate. Schematic showcasing the formation of (c) STO-F1, (d) STOF2, (e) STO-F3 and (f) STO-F4.

Optical properties were measured on oriented assemblies of $SrTiO_3$ for STO-F1-STO-F4 using UV-visible diffuse reflectance spectroscopy (DRS). UV-visible absorption spectra and Tauc plot are shown in Figures S2, ESI. From Figure S2b, ESI, no change in band gap was observed. The bandgap of STO-F1-STO-F4 was calculated to be 3.6 eV which was found to be the same for all the four samples, indicating that the assemblies are active under the UV region of the solar spectrum.

Photocatalytic Hydrogen Evolution

To see the influence of the orientation of the assembly of $SrTiO_3$ nanocubes (formed on a glass substrate (STO-F1-STO-F4)) on the photocatalytic hydrogen evolution activity, the amount of hydrogen evolved from an aqueous solution containing 0.35M Na_2SO_3 (used as hole-scavenger) under 450 W Xenon lamp was measured. No H_2 gas was evolved in the absence of light. Temporal hydrogen evolution under light is shown in Figure 6. The apparent quantum yield was calculated using equation 2 and is tabulated in Table 1. It was observed that the hydrogen evolution activity of STO-F2 (Figure 6a) was the highest amongst the four kinds of assembly viz. STO-F1, STO-F2, STO-F3, and STO-F4. The rate of hydrogen evolution reaction was observed to follow the order STO-F2>STO-F3>STO-F1 ≈STO-F4 with a maximum rate of 0.456 μmol h^{-1} for STO-F2. STOF2 was shown to have a high degree of preferred orientation of particles for the (200) plane (Figure 3b). Long time cyclic stability for STO-F2 was checked for three sequential cycles of 4 hours each. No significant change in the hydrogen evolution activity was observed for STO-F2 after 3rd cycle when compared with 1st cycle (Figure 6b). The composition and orientation of the film after recyclability studies for STO-F2 was checked using PXRD. No change in the structure and the preferred orientation of the oxide for the (200) plane was observed in STO-F2 (Figure S3a, ESI) indicating that the oriented assemblies of STO-F2 were stable after the photocatalytic cyclic stability studies. The morphology and the nature of assembly for STO-F2, after recyclability studies, was checked using FESEM (Figure S3b, ESI). No change in the morphology and nature of assembly was observed after photocatalytic recyclability studies.

Sample	n (Amount of hydrogen gas evolved after 5 h of the reaction) (mol)	Apparent Quantum Yield (AQY) (%)
STO-F1	1.497×10^{-6}	0.0022
STO-F2	2.283×10^{-6}	0.0034
STO-F3	1.643×10^{-6}	0.0024
STO-F4	1.551×10^{-6}	0.0023

Table 1: Apparent quantum yield for hydrogen evolution using the oriented assembly of $SrTiO_3$ nanoparticles on a glass plate (STO-F1-STO-F4)

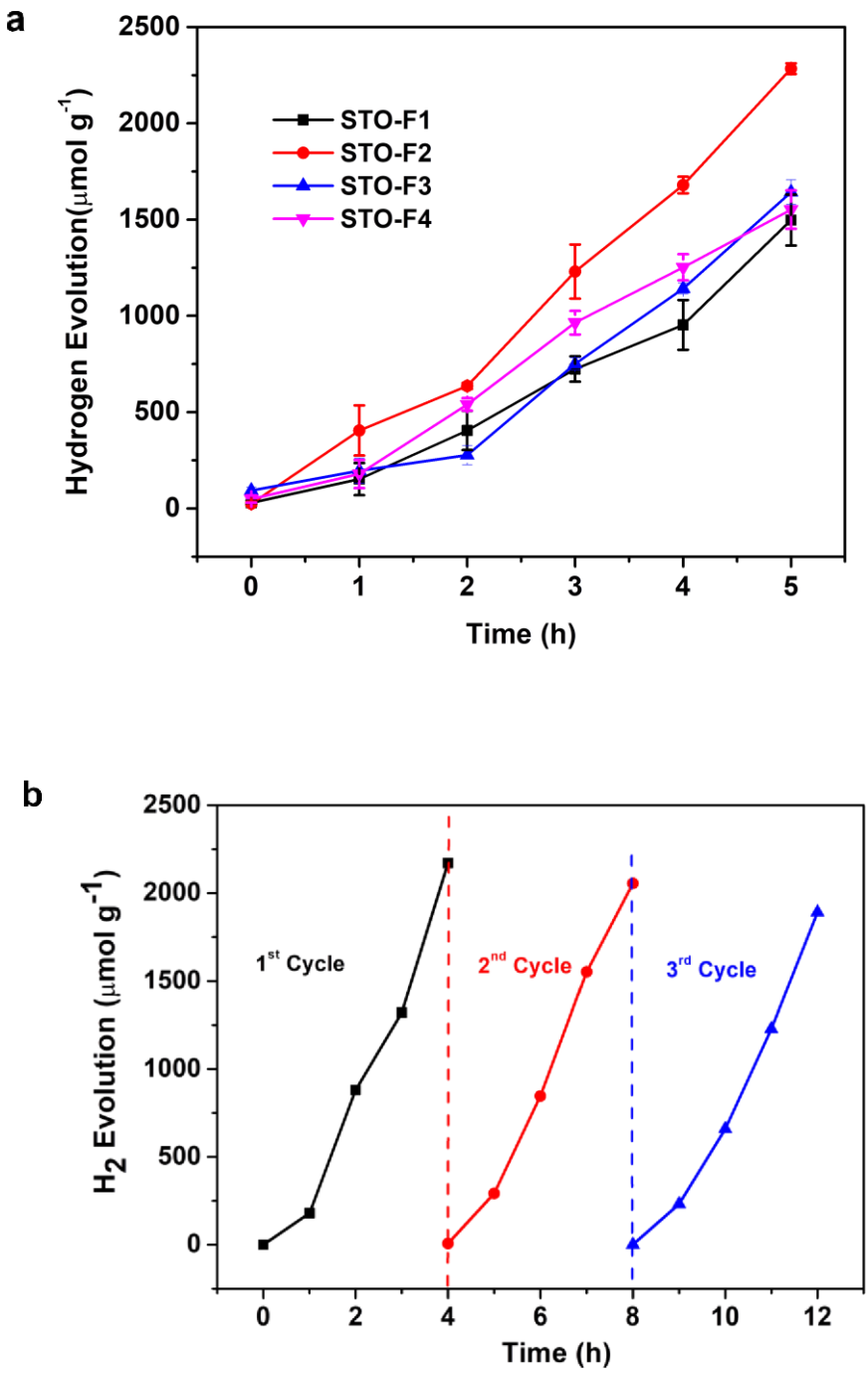

Figure 6: (a) Plot showcasing the amount of hydrogen evolved using $SrTiO_3$ nanostructures deposited on a glass substrate. (b) Recyclability test for three consecutive cycles for STO-F2.

To ensure whether the enhanced activity was due to preferred orientation or local ordered arrangement of particles on the glass substrate, GISAXS studies were carried out on all the samples. From the plots (Figure 7), no local ordering of particles was seen on these assemblies of $SrTiO_3$ on a glass substrate. Thus, it can be deciphered that the (200) orientation of $SrTiO_3$ (in STO-F2) played an important role in the catalytic activity. In addition to the (200) orientation of particles in STO-F2, the deposition of particles over a glass substrate is quite dense and uniform (Figure 4b). So, it is likely that there are large number of particles deposited with a film thickness of ~300 nm and distributed uniformly with (200) plane as the preferred orientation over the glass substrate, that could have resulted in enhanced photocatalytic activity of STO-F2.

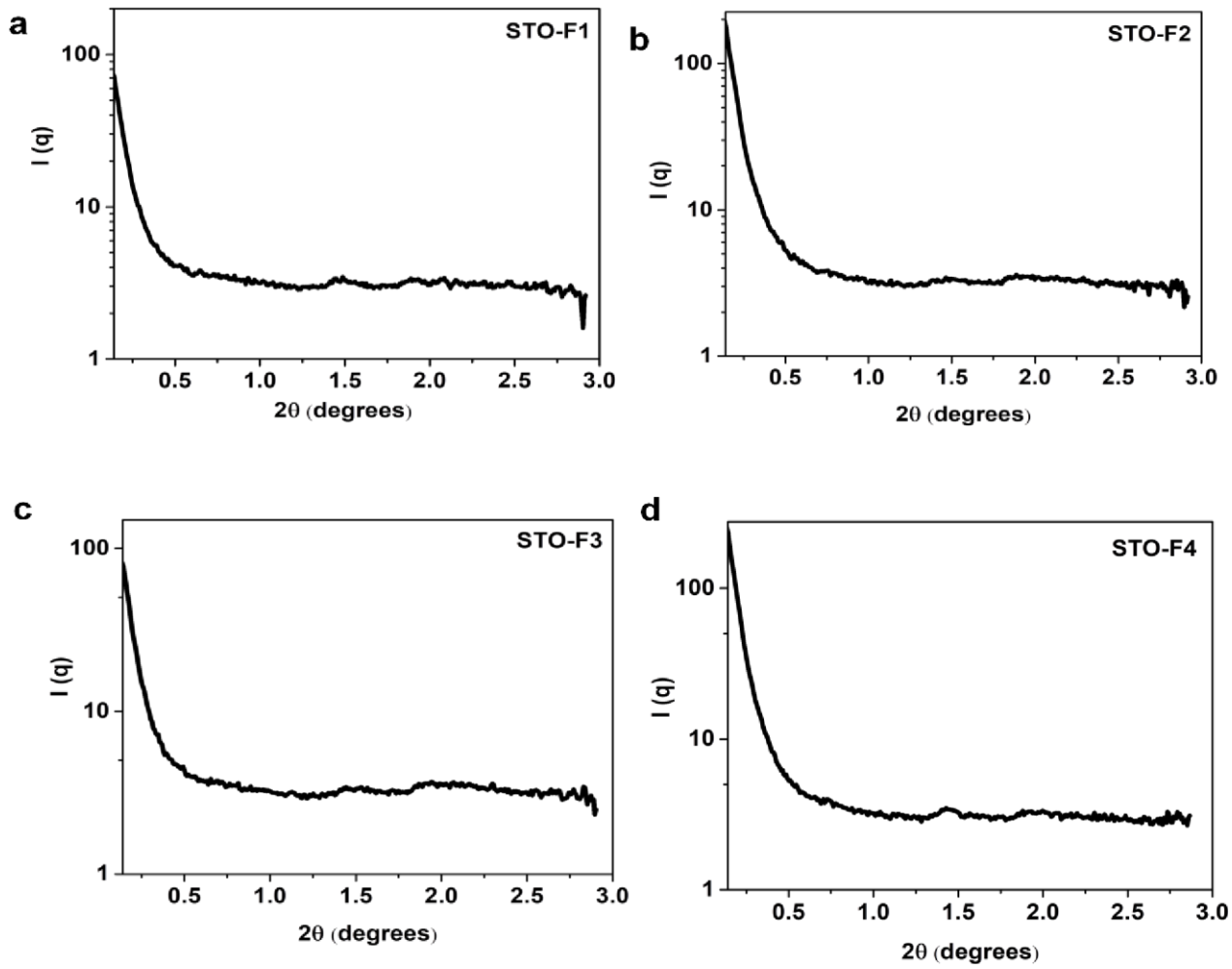

Figure 7: I(q) vs. 2θ plot for (a) STO-F1, (b) STO-F2, (c) STO-F3, and (d) STO-F4.

To gain insights into the H_2 evolution reaction on (100) surface (corresponding to the family of {h00} planes, see experimental section) of $SrTiO_3$ under alkaline conditions ($2H_2O + 2e^- \rightarrow H_2 +$

$2OH^-$), density functional theory calculations involving the nudged elastic band method were performed. In principle, both SrO- and TiO_2 terminations could be catalytically active toward H_2 production. However, we found that the adsorption energy of OH^- on the SrO- termination to be -1.91 eV (-2.31 eV when OH* is adsorbed next to a H*). This value indicates that the desorption of OH^- from the SrO- termination would be difficult, which can cause poisoning of the active sites[24]. In contrast, OH^- is adsorbed with the energy of -1.28 eV (-1.09 eV when OH* is adsorbed next to a H*) on the TiO_2 terminated surface. Thus, the comparison between the two adsorption energies suggests that the regeneration of the catalyst is only possible with TiO_2 termination, which, therefore, will be the subject of our next discussion. It was calculated that the energy of adsorption of an intact water molecule on top of a Ti atom on the reduced TiO_2 terminated surface (Figure S4, ESI) is -0.91 eV, similar to what has been reported for an uncharged TiO_2 termination [25]. From this configuration, we found that the dissociation of water is thermodynamically favored by 0.40 eV, with a remarkably low energy barrier of 0.05 eV. After the dissociation of water ($H_2O + e^- \rightarrow H^* + OH^-$), and the adsorption of a second water molecule on a reduced surface, we focussed on two subsequent pathways[26] (step 1 and step 2) for the formation of H_2, i.e.

Step 1: $H_2O + H^* + e^- \rightarrow H_2 + OH^-$

Step 2: $H^* + H^* \rightarrow H_2$

Figure 8 illustrates that both steps have prohibitively high activation energies, with values between 2.5 and 2.9 eV consistent with those reported[27] for the RuO_2-terminated surface of $SrRuO_3$. While we do not expect the stoichiometric TiO_2-terminated surface to have any appreciable photocatalytic activity towards the formation of H_2, it is well known that $SrTiO_3$ nanostructures contain several defects with oxygen vacancies among the most common ones [19, 28]. This was also confirmed by the XPS studies of nanocubes of $SrTiO_3$ (Figure 2) which prompted us to explore the effect of oxygen vacancies on the formation of H_2. We found that the adsorption energy of a H atom at an oxygen vacancy (Figure S5, ESI) is less than 0.01 eV, i.e. neither too weak nor too strong, and thus ideal for photocatalytic HER[26]. Thus, we adsorbed a dissociated water molecule near the H atom, filling the vacancy, and focussed on step 2 as shown in Figure 9. We observed that the formation of H_2 is exothermic by 0.40 eV. Crucially, the corresponding activation energy of 0.75 eV is significantly lower than those reported above for the clean surface. Based on these results, we predict that the oxygen vacancies of $SrTiO_3$ (possibly together with other types of defects) are the

key sites for the photocatalytic H_2 production on the TiO_2 terminated (100) surface of $SrTiO_3$. It is known[29] that the (110) surface of $SrTiO_3$, formed by alternating $(SrTiO)^{4+}$ and $(O_2)^{4-}$ planes, is polar. However, the polarity is compensated by a (4 × 1) surface reconstruction consisting of corner-sharing TiO_4 tetrahedral which are inert towards the adsorption of water, as shown by a combined experimental and theoretical investigation[30]. Thus, the weak adsorption of water on the (110) surface could be the reason for observing low photocatalytic activity for other assemblies of $SrTiO_3$.

Thus, synergism of deposition of a large number of nanostructures with a preferred (200) crystallographic plane as the exposed surface in STO-F2 and the presence of oxygen vacancies were found to play a key role in enhancing the photocatalytic performance of the nanocubes of $SrTiO_3$.

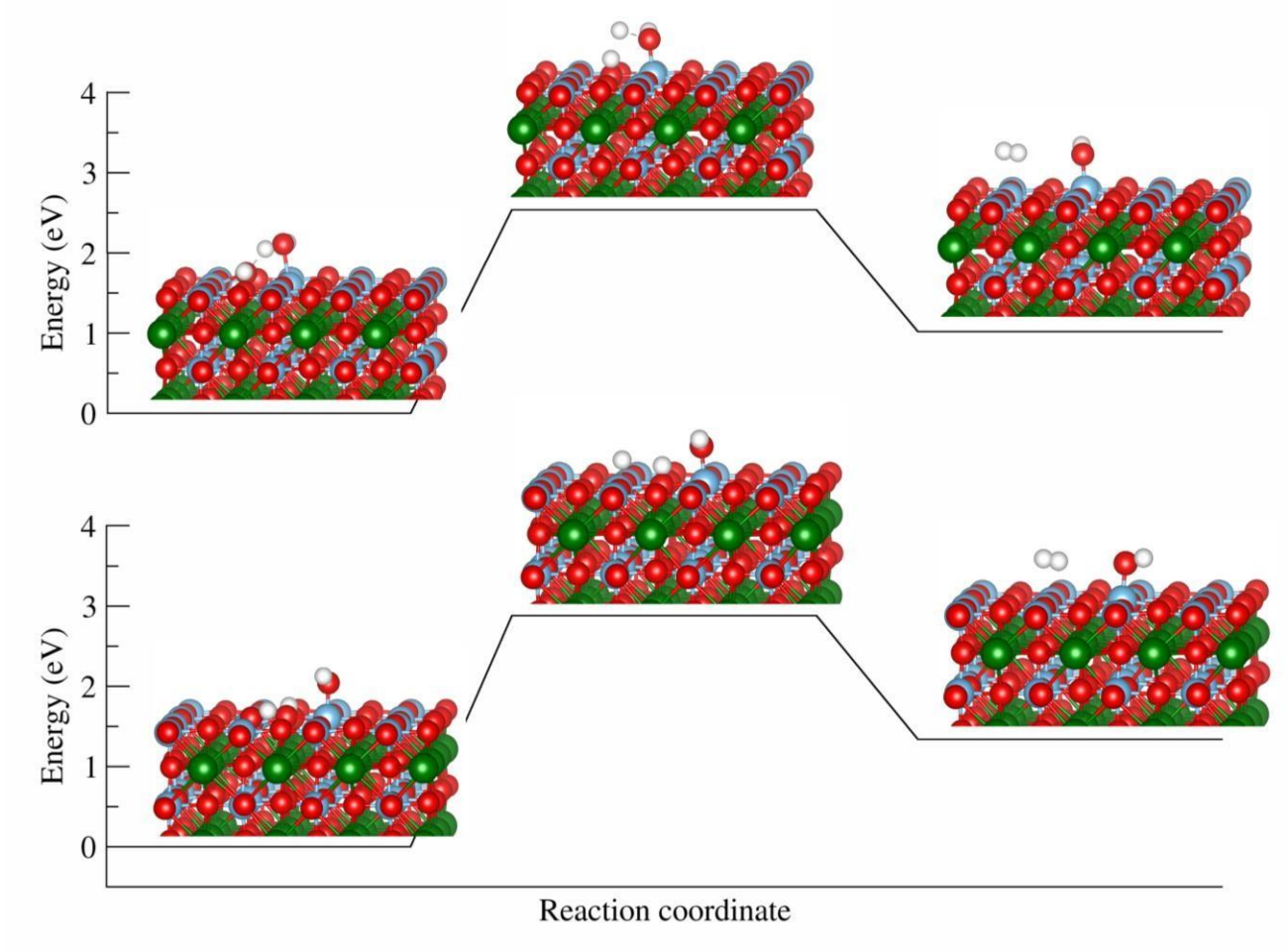

Figure 8: Reaction pathways (a) Step 1 and (b) Step 2 for the formation of H_2 at the (100) surface of $SrTiO_3$. Blue, Green, Red, and White colour is used for depicting Ti, Sr, O, and H atom.

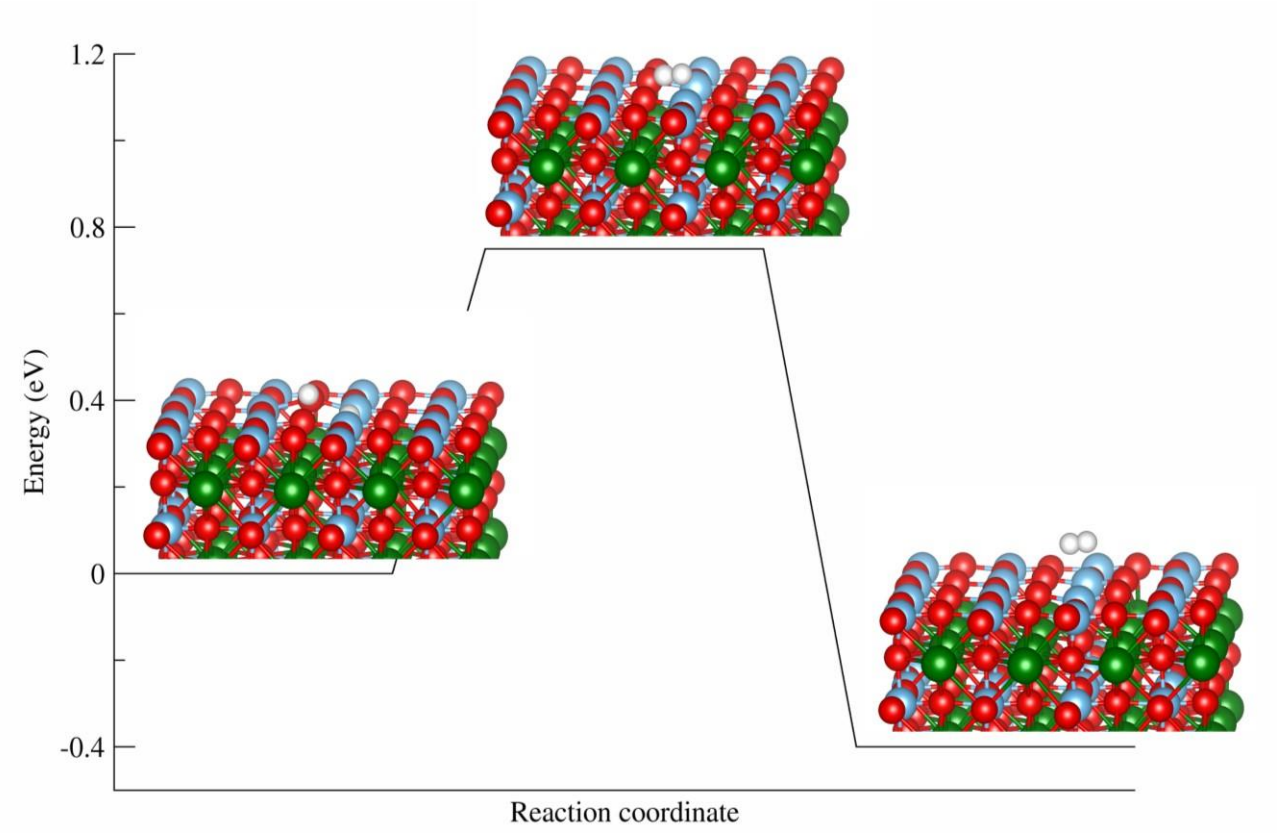

Figure 9: Formation of H_2 at the O vacancy site of the (100) surface of $SrTiO_3$. Blue, Green, Red, and White colour is used for depicting Ti, Sr, O, and H atom.

Conclusion

We have synthesized assemblies of $SrTiO_3$ nanostructures on the glass substrate under different conditions wherein IPTMS was used as a linker between $SrTiO_3$ nanostructures and the glass substrate. It was observed that the nanocubes were orientated along the (200) plane in STO-F1 and STO-F2 wherein the glass substrate was functionalized with IPTMS. From the FESEM study, a uniform layer with high coverage of $SrTiO_3$ nanostructures on the glass substrate was observed for STO-F2 as compared to other samples. The photocatalytic hydrogen evolution activity was observed to be highest in STO-F2 (0.456 μmol h^{-1}). Results of photocatalytic hydrogen evolution were explained based on the orientation of a large number of particles having (200) as the preferred orientation in STO-F2. From the theoretical studies, it was concluded that the oxygen vacancies

of $SrTiO_3$ (possibly together with other types of defects) are the key sites for the photocatalytic H_2 evolution on the TiO_2 terminated (100) surface of $SrTiO_3$. Thus, our work demonstrates the role of oriented assemblies along a preferred crystal plane in enhancing photocatalytic hydrogen activity.

Experimental

Materials and Methods

Strontium nitrate [($Sr(NO_3)_2$), 99%], Methanol (ACS grade), Toluene (≥ 99.9 %,) Ethanol (> 99%) and Sodium hydroxide [(NaOH) (≥ 97%)] were purchased from Merck. Titanium tetraisopropoxide (TTIP) (97%), 3-iodopropyltrimethoxy silane (≥95%) (IPTMS) and sodium sulfite (98%) were purchased from Sigma-Aldrich.

Synthesis of $SrTiO_3$ nanostructures

Strontium Titanate, $SrTiO_3$ was synthesized using the hydrothermal process as reported previously[19] wherein water was taken as a solvent during the synthesis. Briefly, 1.48 mL of titanium tetraisopropoxide was added to 30 mL of water followed by the addition of 1.058 g of strontium nitrate. To this 5 mL of 5 M NaOH solution was added dropwise to obtain a suspension of white precipitates. The reaction mixture (volume of the final mixture was maintained at 35 mL) was then sealed in a 50 mL Teflon-lined stainless steel vessel and heated at 180° C for 24 h. The resultant precipitates were washed several times with distilled water and absolute ethanol and dried at 80°C for 8h.

Different methods were adopted for the synthesis of oriented assemblies of $SrTiO_3$ on the glass substrate, as discussed below.

Functionalization of Glass Substrate

The procedure was followed as reported in the literature. [23] The glass substrate (size 2 cm X 1.5 cm) was washed with HCl (35%) followed by deionized water (DI water) and iso-propanol. These were dried with nitrogen gas. For functionalization of the glass substrate, the dried substrates were immersed in a 5 mL solution of toluene containing 98µL of IPTMS. The solution containing the glass substrate was refluxed at 70 °C under a nitrogen atmosphere. The functionalized glass substrates were washed with toluene to removed excess IPTMS.

Functionalization of $SrTiO_3$ nanostructures

For functionalization of $SrTiO_3$, 30 mg of $SrTiO_3$ nanostructures were dispersed in 30 mL of ethanol solution containing 587µL of IPTMS. This dispersion containing the nanostructures was stirred for 24 h at 40ºC. The particles were then centrifuged and washed with ethanol and dried at 60 ºC.

Assembling $SrTiO_3$ on a glass substrate

The methodology was followed as reported in the literature [23] with some modifications. 5mg of $SrTiO_3$ powder (functionalized/non-functionalized) was dispersed in 5 mL toluene using ultrasonication for 3 hours. The glass substrate (functionalized/non-functionalized) was immersed in the above dispersion. The system was sonicated for 10 minutes. The glass substrate with $SrTiO_3$ deposited over, was then immersed in toluene and sonicated for 10 seconds, to remove extra particles that might be adsorbed on the substrate. The $SrTiO_3$ coated glass substrates were then dried by flushing using a nitrogen gun.

Four different conditions were used for depositing $SrTiO_3$ on a glass substrate. These have been discussed as follows:

STO-F1: In this, both $SrTiO_3$ powder used for the formation of the assembly and the glass substrate were functionalized with IPTMS.

STO-F2: In this, the glass substrate was functionalized with IPTMS while $SrTiO_3$ powder that was used for the formation of the assembly was not functionalized.

STO-F3: In this, $SrTiO_3$ powder that was used for the formation of the assembly was functionalized with IPTMS while the glass substrate was not functionalized.

STO-F4: In this, neither the glass substrate nor $SrTiO_3$ powder that was used for the formation of the assembly was functionalized with IPTMS.

For obtaining the amount of oxide deposited on the glass substrate, the remaining dispersion containing $SrTiO_3$ (after removal of oxide coated substrate) was centrifuged, washed, dried and weighed. Based on this, it was found that ~ 1 mg of the oxide was deposited on the glass substrate. This amount was used for the calculation of the amount of hydrogen evolution per gram for STOF1-STO-F4.

Characterization

The phase purity of the synthesized $SrTiO_3$ and the orientation of $SrTiO_3$ powder on the glass substrate (STO-F1-STO-F4) were checked using powder X-ray diffraction (PXRD, Bruker D8 Advance Eco) with Cu Kα as the X-ray source (λ = 0.15406 nm). The XRD instrument was operated at 40 kV and 25 mA at scanning steps of 0.0103 with a step time of 0.3 s/step in the 2θ range of 10−80°. Transmission electron microscope studies (TEM) studies were carried out on JEOL, JEM-2100 operated at an accelerating voltage of 200 kV. $SrTiO_3$ powder was dispersed in ethanol and drop-casted on a carbon-coated copper grid. Field Emission Scanning Electron Microscopy (FESEM) studies were carried out on JEOL JSM-7610F Plus. XPS (X-Ray Photoelectron Spectroscopy) studies were carried out on Thermo Scientific's K-alpha X-ray Photoelectron Spectrometer (XPS) system with the following settings: step: 0.05 eV, time per step: 1s, and the number of cycles: 5, Source Al k-alpha-1486eV. GISAXS studies were carried out on Xeuss SAXS/WAXS System (Model C HP100 fm) with Cu Kα as the X-ray source (λ = 0.154 nm) and sample-to-detector distance: 1346.68 mm. Diffuse Reflectance Spectra were collected on a UV–visible spectrophotometer, Shimadzu UV-2600, in a wavelength range of 200-800 nm. The absorption of the materials from the reflectance spectra, in the wavelength range, was obtained using Kubelka-Munk's (K-M) function. The bandgap was calculated using the Tauc equation (equation 1).

$$(\alpha h\upsilon)^{\frac{1}{n}} = C(h\upsilon - E_g) \qquad \text{-------- (1)}$$

where α is the absorption coefficient; E_g is the bandgap of the material; n denotes the nature of transition (n = ½ for direct transition and n = 2 for indirect transition).

Photocatalytic Hydrogen Evolution Reaction (HER)

A top irradiation quartz reactor of capacity 140 mL was used for the photocatalytic hydrogen evolution reaction. The assemblies of particles on a glass substrate were immersed in a 40 mL of 0.35M aqueous solution of Na_2SO_3. The reaction was carried out in absence of any metal cocatalyst to see the direct influence of the oriented assembly of $SrTiO_3$ on the photocatalytic performance. The dissolved oxygen was eliminated by purging N_2 gas for 30 minutes. Xe lamp (450W) was used as the source of light. Ray virtual radiation actinometer, Newport, Model 91150V was used to obtain the photon flux of the Xe lamp. The hydrogen gas evolved during the reaction was analyzed

at an interval of 1 h using gas chromatography (GC, Perkin Elmer Clarus 680) with a thermal conductivity detector. The apparent quantum efficiency was calculated using the equation 2.

$$AQY = \frac{2nN_Ahc}{PS\lambda t} \times 100 \quad \text{... ... ... (2)}$$

where n : amount of hydrogen evolved; N_A : Avogadro's constant (6.022×10^{23} mol^{-1}); h: Planck's constant (6.63×10^{-34} J s); c: speed of the light (3×10^{10} cm/s); P: power density of the incident light (181×10^{-3} W/cm^2); S: irradiation area (12.6 cm^2); λ: representative wavelength of the incident light (using the radiation spectrum of the lamp, 390 nm (390×10^{-7} cm)); and t: time duration of the incident light (18000 s).

Computational details

Given that all {h00} planes of a crystal are parallel to the (100) plane, (100) and (200) indicate the same surface orientation. The reflection from (200) has much larger intensity than that from (100) (see Figure 3), and therefore, for consistency with our XRD data, we have used (200) to indicate the plane orientation. We have instead chosen the (100) Miller indices in explaining the H_2 evolution using DFT, in line with the computational literature on $SrTiO_3$. The two (100) surface terminations (corresponding to the family of {h00} planes) of $SrTiO_3$, i.e. the SrO- and TiO_2 terminated surfaces (Figure S6, ESI) were built from an optimized 1 × 1 × 1 bulk unit cell of $SrTiO_3$ with a lattice constant of 3.953 Å[31]. The unit cell was replicated along x, y, and z into a 4 × 4 × 4 supercell. A vacuum region of at least 40 Å along the normal direction was then added to ensure energy convergence of the charged supercells. All density functional theory calculations were performed with the QUICKSTEP program of CP2K[32], PBE exchange-correlation functional[33], the DZVP-MOLOPT basis set[34], and the GTH pseudopotentials[35] proposed by Goedecker, Teter, and Hutter. The calculations were done at the Γ-point with a plane wave cutoff of 800 Ry. The structures were optimized with a limited memory algorithm (LBFGS)[36]. During optimizations, the bottom $SrTiO_3$ layer was kept fixed. Transition states were located with the climbing image nudged elastic band algorithm[37], using ten images.

Conflicts of interest

There are no conflicts to declare.

Acknowledgement

AV thanks INST, Mohali for the fellowship. SV thanks CSIR (01(2943)/18-EMR-II), Govt. of India for funding. AV and SV thank Dr. Santanu Kumar Pal, IISER Mohali for GISAXS studies.

Via U.T.'s membership of the UK's HEC Materials Chemistry Consortium funded by EPSRC (EP/L000202, EP/R029431), this work used the ARCHER2 UK National Supercomputing Service (http://www.archer2.ac.uk).

Keywords: Exposed Surfaces; Hydrogen Evolution Reaction; Oriented Assemblies; Photocatalysis

References

[1] (a) K. Maeda, K. Teramura, D. Lu, T. Takata, N. Saito, Y. Inoue, K. Domen, *Nature* **2006**, *440*, 295; (b) K. Maeda, *J. Photochem. Photobio. C: Photochem. Rev.* **2011**, *12*, 237-268. [2] H. Tong, S. Ouyang, Y. Bi, N. Umezawa, M. Oshikiri, J. Ye, *Adv. Mater.* **2012**, *24*, 229251.

[3] (a) N. M. Flores, U. Pal, R. Galeazzi, A. Sandoval, *RSC Adv.* **2014**, *4*, 41099-41110; (b) L. Zhang, T. Xu, X. Zhao, Y. Zhu, *Appl. Catal. B: Environ.* **2010**, *98*, 138-146.

[4] S. Bai, W. Jiang, Z. Li, Y. Xiong, *ChemNanoMat* **2015**, *1*, 223-239.

[5] B. Wang, S. Shen, L. Guo, *ChemCatChem* **2016**, *8*, 798-804.

[6] Q. Kuang, S. Yang, *ACS Appl. Mater. Interfaces* **2013**, *5*, 3683-3690.

[7] P. A. Morris Hotsenpiller, J. D. Bolt, W. E. Farneth, J. B. Lowekamp, G. S. Rohrer, *J. Phys. Chem. B* **1998**, *102*, 3216-3226.

[8] G. Li, T. Varga, P. Yan, Z. Wang, C. Wang, S. A. Chambers, Y. Du, *Phys. Chem. Chem. Phys.* **2015**, *17*, 15119-15123.

[9] G. Li, Z. Yi, Y. Bai, W. Zhang, H. Zhang, *Dalton Trans.* **2012**, *41*, 10194-10198.

[10] L. Jiang, Y. Zhang, Y. Qiu, Z. Yi, *RSC Adv.* **2014**, *4*, 3165-3170.

[11] S. Yamazoe, H. Sakurai, M. Fukada, H. Adachi, T. Wada, *Appl. Phys. Lett.* **2009**, *95*, 062906.

[12] C. Zhang, T. Uchikoshi, T. Ishigaki, *Adv. Powder Technol.* **2021**, *32*, 4149-4154.

[13] D. Li, Y. Liu, W. Shi, C. Shao, S. Wang, C. Ding, T. Liu, F. Fan, J. Shi, C. Li, *ACS Energy Lett.* **2019**, *4*, 825-831.

[14] K. M. Macounová, R. Nebel, M. Klusáčková, M. Klementová, P. Krtil, *ACS Appl. Mater. Interfaces* **2019**, *11*, 16506-16516.

[15] P.-L. Hsieh, G. Naresh, Y.-S. Huang, C.-W. Tsao, Y.-J. Hsu, L.-J. Chen, M. H. Huang, *J. Phys. Chem. C* **2019**, *123*, 13664-13671.

[16] Z. Wu, Y. Zhang, X. Wang, Z. Zou, *New J. Chem.* **2017**, *41*, 5678-5687.

[17] M. Zhou, J. Chen, Y. Zhang, M. Jiang, S. Xu, Q. Liang, Z. Li, *J. Alloys Compd.* **2020**, *817*, 152796.

[18] X. Wu, X. Wang, J. Li, G. Zhang, *J. Mater. Chem. A* **2017**, *5*, 23822-23830.

[19] A. Vijay, S. Vaidya, *ACS Appl. Nano Mater.* **2021**, *4*, 3406-3415.

[20] B. Bharti, S. Kumar, H.-N. Lee, R. Kumar, *Sci. Rep.* **2016**, *6*, 32355.

[21] X. Zhang, H. Tian, X. Wang, G. Xue, Z. Tian, J. Zhang, S. Yuan, T. Yu, Z. Zou, *Mater. Lett.* **2013**, *100*, 51-53.

[22] H. Tan, Z. Zhao, W.-b. Zhu, E. N. Coker, B. Li, M. Zheng, W. Yu, H. Fan, Z. Sun, *ACS Appl. Mater. Interfaces* **2014**, *6*, 19184-19190.

[23] G. Ma, T. Takata, M. Katayama, F. Zhang, Y. Moriya, K. Takanabe, J. Kubota, K. Domen, *CrystEngComm* **2012**, *14*, 59-62.

[24] N. Mahmood, Y. Yao, J.-W. Zhang, L. Pan, X. Zhang, J.-J. Zou, *Adv. Sci.* **2018**, *5*, 1700464.

[25] (a) L.-Q. Wang, K. F. Ferris, S. Azad, M. H. Engelhard, *J. Phys. Chem. B* **2005**, *109*, 45074513; (b) J. D. Baniecki, M. Ishii, K. Kurihara, K. Yamanaka, T. Yano, K. Shinozaki, T.
Imada, Y. Kobayashi, *J. Appl. Phys.* **2009**, *106*, 054109.

[26] J. Dai, Y. Zhu, H. A. Tahini, Q. Lin, Y. Chen, D. Guan, C. Zhou, Z. Hu, H.-J. Lin, T.-S. Chan, C.-T. Chen, S. C. Smith, H. Wang, W. Zhou, Z. Shao, *Nat. Commun.* **2020**, *11*, 5657.

[27] Y. Zhu, H. A. Tahini, Z. Hu, J. Dai, Y. Chen, H. Sun, W. Zhou, M. Liu, S. C. Smith, H. Wang, Z. Shao, *Nat. Commun.* **2019**, *10*, 149.

[28] (a) A. E. Souza, G. T. A. Santos, B. C. Barra, W. D. Macedo, S. R. Teixeira, C. M. Santos, A. M. O. R. Senos, L. Amaral, E. Longo, *Cryst. Growth Des.* **2012**, *12*, 5671-5679; (b) K.

Eom, E. Choi, M. Choi, S. Han, H. Zhou, J. Lee, *J. Phys. Chem. Lett.* **2017**, *8*, 3500-3505.
[29] F. Bottin, F. Finocchi, C. Noguera, *Surf. Sci.* **2005**, *574*, 65-76.
[30] Z. Wang, X. Hao, S. Gerhold, Z. Novotny, C. Franchini, E. McDermott, K. Schulte, M. Schmid, U. Diebold, *J. Phys. Chem. C* **2013**, *117*, 26060-26069.
[31] U. Terranova, F. Viñes, N. H. de Leeuw, F. Illas, *J. Mater. Chem. A* **2020**, *8*, 9392-9398.
[32] T. D. Kühne, M. Iannuzzi, M. D. Ben, V. V. Rybkin, P. Seewald, F. Stein, T. Laino, R. Z. Khaliullin, O. Schütt, F. Schiffmann, D. Golze, J. Wilhelm, S. Chulkov, M. H. BaniHashemian, V. Weber, U. Borštnik, M. Taillefumier, A. S. Jakobovits, A. Lazzaro, H. Pabst, T. Müller, R. Schade, M. Guidon, S. Andermatt, N. Holmberg, G. K. Schenter, A. Hehn, A. Bussy, F. Belleflamme, G. Tabacchi, A. Glöß, M. Lass, I. Bethune, C. J. Mundy, C. Plessl, M. Watkins, J. VandeVondele, M. Krack, J. Hutter, *J. Chem. Phys.* **2020**, *152*, 194103.
[33] J. P. Perdew, K. Burke, M. Ernzerhof, *Phys. Rev. Lett.* **1996**, *77*, 3865-3868.
[34] J. VandeVondele, J. Hutter, *J. Chem. Phys.* **2007**, *127*, 114105.
[35] S. Goedecker, M. Teter, J. Hutter, *Phys. Rev. B* **1996**, *54*, 1703-1710.
[36] R. H. Byrd, P. Lu, J. Nocedal, C. Zhu, *SIAM J. Sci. Comput.* **1995**, *16*, 1190-1208.
[37] G. Henkelman, B. P. Uberuaga, H. Jónsson, *J. Chem. Phys.* **2000**, *113*, 9901-9904.

Table of Content

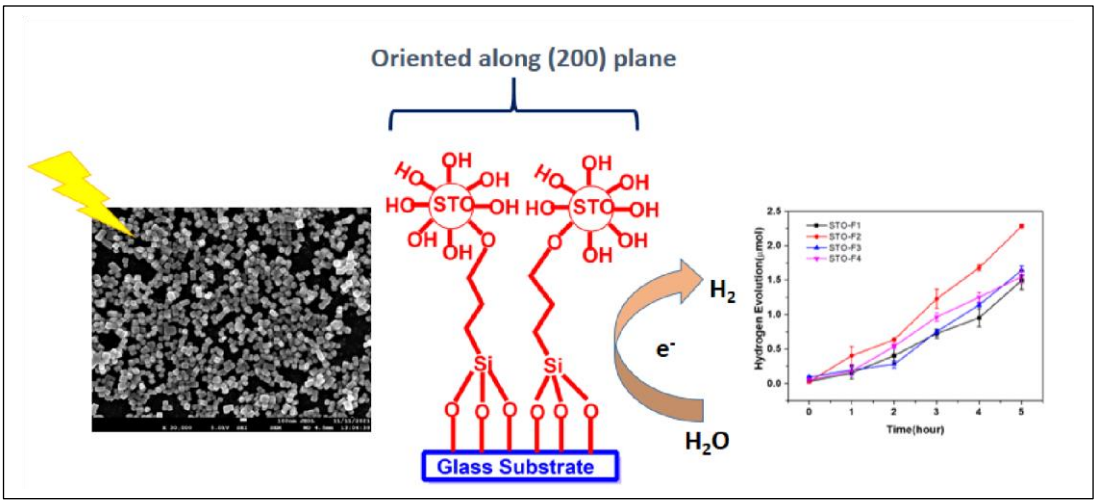

Orientation of assembly of nanostructures affects photocatalytic hydrogen evolution reaction.